DOI 10.24425/aee.2023.146050

Robust microgrids for distribution systems with high solar photovoltaic penetration

W.E.P. Sampath Ediriweera[1] ✉, **N.W.A. Lidula**[1], **H. Dayan B.P. Herath**[2]

[1]*Department of Electrical Engineering, University of Moratuwa*
Moratuwa, Sri Lanka

[2]*Colombo City, Ceylon Electricity Board*
Sri Lanka

e-mail: {✉*ediriweeraweps.21/lidulan}@uom.lk, {ediriweera.sampath/dayan85}@gmail.com*

(Received: 03.03.2023, revised: 21.06.2023)

Abstract: A microgrid is an appropriate concept for urban areas with high penetration of renewable power generation, which improves the reliability and efficiency of the distribution network at the consumer premises to meet various loads such as domestic, industrial, and agricultural types. Microgrids comprising inverter-based and synchronous generator-based distribution generators can lead to the instability of the system during the islanded mode of operation. This paper presents a study on designing stable microgrids to facilitate higher penetration of solar power generation into a distribution network. A generalized small signal model is derived for a microgrid with static loads, dynamic loads, energy storages, solar photovoltaic (PV) systems, and diesel generators, incorporating the features of dynamic systems. The model is validated by comparing the transient curves given by the model and a transient simulator subjected to step changes. The result shows that full dynamic models of complex systems of microgrids can be built accurately, and the proposed microgrid is stable for all the considered loading situations and solar PV penetration levels according to the small signal stability analysis.

Key words: converter, dynamic system, robustness, stability, synchronous generators

1. Introduction

Nomenclature

V_{odq} d and q-axis voltage of the capacitor of the LC filter of the considered inverter,
ω_{com} common frequency,
I_{idq} d and q-axis current on the inverter side of the considered inverter,

I_{odq} d and q-axis axis grid side current of the considered inverter,
V_{bdq} d and q-axis voltage of inverter at grid connecting point,
V_{idq*} d and q-axis axis desired voltage on the inverter side of the considered inverter,
I_{idq*} d and q-axis axis desired current on the inverter side of the considered inverter,
δ angle of the individual reference with respect to the common reference frame.

The concern for sustainable energy growth has increased due to global warming and environmental pollution, and renewable power generation has been considered a means to satisfy the increasing energy demand. Renewable power generation sources such as solar photovoltaic (PV) arrays, micro wind turbines, biomass power plants, and fuel cells can be connected to the distribution network locally, and such generations are called distributed generations (DGs). Microgrids with smart and intelligent features have been emerging to facilitate the high penetration of renewable power integration into the distribution network of urban and rural areas [1].

However, before the practical implementation of microgrids, during the design stage, it is essential to make sure that the system is highly robust under all operating conditions. Its ability to respond to changing operating conditions is considered an essential aspect of microgrid development. Microgrid stability can be classified as: 1) transient stability, 2) voltage stability, and 3) small signal stability, for the purpose of analysis. Most of the reported studies on microgrids planning have given comparatively less importance to transient stability analysis; the reasons would include, less penetration of synchronous machines based DGs than inverter-based sources and relatively small capacities of DGs.

However, inverter-based distributed generation having less, or nil physical inertia can lead to system collapse even under small perturbations in the system based on the adopted control architecture [2, 3]. Voltage stability comes into action due to reactive power limits and operations of tap changes. Also, the lack of system damping can result in undamped oscillatory states with small disturbances such as load changes and parameter changes. Both static and dynamic loads can be found in the power system, and static loads do not affect the stability of the microgrids. However, dynamic loads consider the historical data to generate the present state and therefore can affect the system stability. Also, induction motor-based loads can affect the inertia and damping of the system [4, 5]. Therefore, a comprehensive analysis of the small signal stability of microgrids is a crucial requirement to ensure the stable operation of microgrids [6, 7].

The effect of the dynamic loads on the stability of the microgrids with parallel connected inverters is studied in [8–10] and [11]. It is shown that the stability of the microgrids increases when the damping and inertia increase, and system stability is affected by dynamic loads compared to the static loads. However, the effect of the grid following converters and synchronous machines on stability has not been studied in [8] and [9]. Also, the stability has been verified only on a single operating point [12, 13], and therefore, stability for all the operating points cannot be guaranteed. In a study conducted on a islanded microgrid with synchronous generators and grid-forming inverters, the optimal placement of distributed energy resources (DER) is obtained with the aid of a robustness matrix, which corresponds to a state matrix given by the small signal analysis [14]. However, in this study, the dynamics of the control loops of the grid-forming inverters have been neglected. Also, the dynamics of the rotor and stator of the synchronous generators have been simplified, and the dynamic behavior of the loads has not been considered.

The impact of the grid-forming converters on the small-signal stability of power systems that are integrated with a phase-locked loop (PLL)-based converters, which assume ideal power

sources, is investigated in [15]. Based on the matrix perturbation theory, it is revealed that the placement of grid-forming inverters in the optimal grid location can increase the stability, and strength of the power grid. However, the study does not reflect a microgrid, but the stability of a part of the distribution network with high penetration of inverter based DGs. According to [16] and [17], microgrids' stability is influenced by the grid-forming inverters' control parameters. The study presented in [16] is conducted to derive a small signal model to analyze the autonomous operation of inverter-based microgrids. It has been observed that low-frequency modes are susceptible to network configuration and parameters of power controller dynamics of DGs. In contrast, high-frequency modes are susceptible to inverter inner loop dynamics, network dynamics, and load dynamics. Experimental results have been used to verify the results obtained from the model. Another study in [17] has proposed a small signal model for an islanded AC microgrid with distributed secondary control. The eigenvalues have been used to see the effect of control parameters on the stability, and the result shows that the voltage controller supports voltage restoration and reactive power sharing. However, the considered microgrids do not have dynamic loads and grid-following inverters, and only inverter-based energy sources are considered.

The dynamic behaviour of a microgrid is influenced by the gain setting controllers of the inverters, line impedance, and load, as well as the power-sharing level of each DER unit. Despite the fact that the inverter and line parameters remain constant during the primary design stage, the gain setting can have a significant impact on the microgrid performance under different renewable penetration levels [18]. A study presented in [19] on a hybrid renewable model based on droop control to understand the performance of the low-frequency critical modes within the microgrid, demonstrates the improved damping performance of the microgrid with less renewable power generation penetration. According to the study presented in [20], renewable sources participating in the frequency regulation of a microgrid can significantly improve the dynamics of the microgrid. To improve the power response of the microgrid, a study presented in [12] proposes an anti-droop controller for each converter in the microgrid. Based on the small signal stability analysis, it is demonstrated that inverters integrated with droop control for power sharing provide more room for adjusting the eigenvalues to improve response of the microgrid. However, the presented studies did not investigate the effect of renewable energy sources operated with constant active and reactive power modes on the small signal stability of microgrids.

In summary, due to the intermittency associated with renewable power generation sources such as solar PV and the high-cost factor associated with energy storage, microgrids in island operation should be equipped with diesel generators to increase their resilience. However, most of the microgrids subjected to stability analysis are not equipped with any such backup generation. Also, the studies that consider the synchronous machine-based generators in microgrids use simplified models of DERs [14], and models do not represent the correct dynamic behaviour of the rotor and stator. Recently, many studies have considered the effect of the control parameters on the stability of microgrids with grid-forming inverters [13, 16, 17]. Additionally, some critical aspects related to practical microgrids have not been considered, such as load profile and solar profile [8, 9, 12–14]. Furthermore, to the best of the author's knowledge, most studies only analyze the penetration of renewable sources equipped with droop control on the small signal stability. This paper presents a generalized small signal model developed for a microgrid consisting of

dynamic loads, rooftop solar PV systems, energy storages, and diesel generators to analyze the stability of a proposed microgrid for all load conditions and different levels of solar PV penetration throughout the day. In the islanded operation, the diesel generator and the solar PV system work on the grid following constant active power control mode while energy storage is operated on grid forming mode. An eigenvalue-based analysis is used to determine the effect of loading conditions and the level of solar PV penetration on the small signal stability of the microgrid.

The rest of this paper is organized as follows: Section 2 presents the design details of a microgrid for an existing distribution network. Then, Section 3 presents the details of constructing a generalized state space model for a microgrid with energy storages, solar PV systems, and diesel generators. Section 4 illustrates the validation of the proposed model by comparing the transient curves given by a transient simulator. Results given by the small signal analysis on the robustness of the microgrid are presented in Section 5. The paper concludes with the conclusion and suggestions for possible future research directions.

2. Location for the study

An existing distribution network in Colombo City, Sri Lanka, was converted into a cluster of microgrids with appropriate integration of DERs to facilitate higher penetration of renewable power generation. Each microgrid in the cluster was designed to be self-sufficient to maintain stability and scalability while the excess energy is transferred to the cluster [21]. Therefore, the sizing was done for a single microgrid in its islanded operation.

In this process, energy balance calculations were performed using the HOMER Pro v13.10 software for a microgrid comprising a PV array, diesel generator, and energy storage.

Figure 1(a) shows the basic configuration of the proposed microgrid with capacities. The energy profile of the microgrid observed on 13th December 2021 with maximum demand is shown in Fig. 1(b).

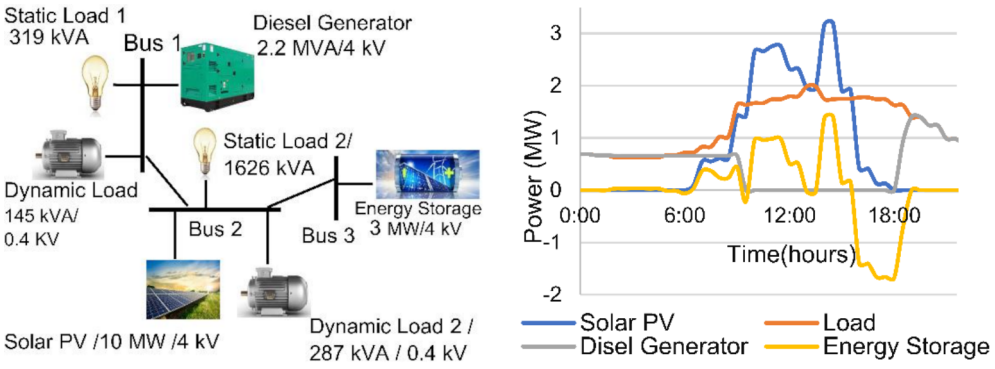

(a) (b)

Fig. 1. Details of the proposed microgrid: the basic configuration (a); energy management (b)

3. State space model of the microgrid

Small or transitory load changes and system damping can cause small perturbations in the system states of the microgrid and can lead to stability problems. Local oscillation can be observed with the interaction of the controls in the microgrids. Therefore, small signal stability of the microgrid should be analyzed in detail as explained in the introduction [22, 23]. The state space-based model is a well-established method of stability analysis by researchers, while the other methods are still in the research stage [24, 25]. Therefore, the state space-based small signal analysis is used in this study.

The complete small-signal state model presented in this article divides the whole system into five major subsystems: 1) solar PV system, 2) energy storage, 3) diesel generator, 4) dynamic load, and 5) network. The solar PV system and the diesel generator work on the grid following PQ mode and energy storage is operated in grid forming mode. Also, modelling a single unit of each DERs and a dynamic load is necessary. Each DER is modelled on each own reference frame. The power variant version of park transformation explained in [26] is used to convert all the quantities of the subsystem from abc reference frame to the individual dq reference frame, which rotates at their individual angular frequencies. Also, the state equations of the loads and the network are defined on the common reference frame. All the other reference frames are transformed to this common reference frame using the transforming technique shown in Fig. 2 and defined in (1) and (2) [21]. Here, the axis set $(D-Q)$ is the common reference frame rotating at a frequency ω_{com}, whereas axes $(d-q)_i$ is the reference frame of i-th converter rotating at ω_i, respectively. Furthermore, the axes $(d-q)_j$ is the reference frame of the j-th diesel generator rotating at ω_j [26, 27].

$$\Delta V_{dqi} = (\partial T_S^{-1}/\partial\delta)V_{DQi} + T_S^{-1}\Delta V_{DQi}\,, \tag{1}$$

$$\Delta I_{DQi} = (\partial T_S/\partial\delta)I_{dqi} + T_S\Delta I_{dqi}\,, \tag{2}$$

where:

$$T_S = \left[\begin{bmatrix}\cos\delta_i & \sin\delta_i\end{bmatrix}^T \quad \begin{bmatrix}-\sin\delta_i & \cos\delta_i\end{bmatrix}^T\right]^T.$$

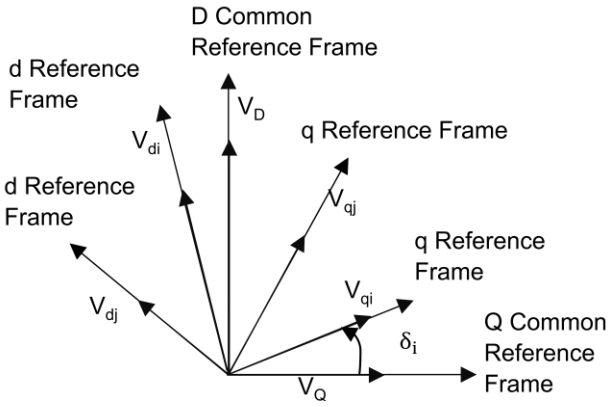

Fig. 2. Reference frame transformation

3.1. Solar PV system

In a microgrid, it is common to export the power generated by solar PV into the network via an inverter by setting a current reference to it and making it operate in the grid feeding mode. Also, the inverter is provided with the DC link voltage from the original energy source. However, the dynamics of the boost converter and maximum power point tracker (MPPT) are neglected, considering ideal current sources. Moreover, the inverter dynamics can be neglected with the realization of high switching frequencies.

The PLL is used to track the frequency of the network and the phase angle of the voltage at the point of the interconnection [21]. This process ensures the alignment of the phase in the direction of the q-axis; therefore, the q-axis voltage is regulated to zero. The PLL is realized as shown in Fig. 3 [28, 29]. The phase detector compares d and q-axis input signals and the output generates the phase and frequency. Equations (3) and (4) represent the dynamic behavior of the PLL illustrated in Fig. 3. Here σ, P_{LL}, ω_0 and ω are the offset angle and integral of the phase error, base frequency, and frequency tracked by PLL block, respectively. Also, V_{od} and V_{oq} are d and q-axis input voltage of the inverter. It is measured across the capacitor of the LC filter of the inverter.

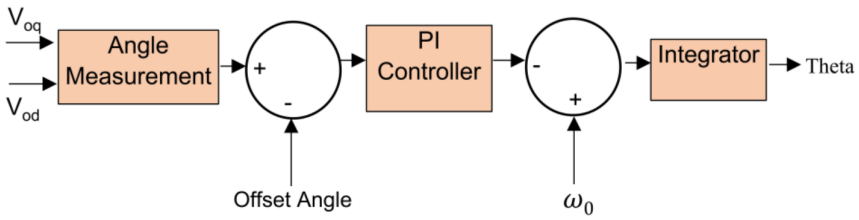

Fig. 3. Block diagram of the phase-locked loop

$$\omega = \omega_0 + K_p(\tan^{-1}(V_{od}/V_{oq}) - \sigma) + K_i P_{LL}, \tag{3}$$

$$\dot{P}_{LL} = (\tan^{-1}(V_{od}/V_{oq}) - \sigma). \tag{4}$$

By linearizing and rearranging the above equations, the small signal model of the PLL block can be written in a state-space form as in (5) and (6).

$$\begin{aligned}\left[\Delta\dot{\delta} \quad \Delta\dot{P}_{LL}\right]^T &= A_{PLLs}\left[\Delta\delta \quad \Delta P_{LL}\right]^T + B_{1PLLs}\Delta\omega_{\text{com}} \\ &\quad + B_{2PLLs}\left[\Delta I_{idq} \quad \Delta V_{odq} \quad \Delta I_{odq}\right]^T, \end{aligned} \tag{5}$$

$$\Delta\omega = C_{PLLs}\left[\Delta\delta \quad \Delta P_{LL}\right]^T + D_{PLLs}\left[\Delta I_{idq} \quad \Delta V_{odq} \quad \Delta I_{odq}\right]^T, \tag{6}$$

where:

$$\boldsymbol{A}_{PLLs} = \begin{bmatrix} 0 & K_i \\ 0 & 0 \end{bmatrix},$$

$$\boldsymbol{B}_{1PLLs} = \begin{bmatrix} -1 \\ 0 \end{bmatrix},$$

$$\boldsymbol{C}_{PLLs} = \begin{bmatrix} 0 & K_i \end{bmatrix},$$

$$\boldsymbol{D}_{PLLs} = \left(1/\left(V_{oq}^2 + V_{od}^2\right)\right)\left[0 \;\; 0 \;\; K_p V_{oq} \;\; -K_p V_{od} \;\; 0 \;\; 0\right],$$

$$\boldsymbol{B}_{2PLLs} = \left(1/\left(V_{oq}^2 + V_{od}^2\right)\right)\left[\left[0 \;\; 0 \;\; K_p V_{oq} \;\; -K_p V_{od} \;\; 0 \;\; 0\right]^T \left[0 \;\; 0 \;\; V_{oq} \;\; -V_{od} \;\; 0 \;\; 0\right]^T\right]^T.$$

The DC-link stability is guaranteed by maintaining the power generated by the solar panel (P_{in}) being equal to the power flowing to the grid (P). Therefore, the active power control is done by maintaining the DC link voltage (V_{DC}) at the reference value. The error between the reference DC-link voltage and the measured DC-link voltage, which is affected by the MPPT to generate the d-axis current reference. Equation (7) illustrates the dynamics of the DC link voltage in terms of the input power and the output power. Instantaneous active power (P^*) and reactive power (Q^*) defined in (8) and (9) are subjected to low pass filtering, and the resultant active (P) and reactive (Q) power is illustrated in (10) and (11) [30]. Here, C_{DC} is the capacitance of the DC link. Also, ω_{C1} and ω_{C2} are cut-off frequencies of corresponding filters.

$$\dot{V}_{\text{DC}} = (1/C_{\text{DC}}V_{\text{DC}})(P_{\text{in}} - P), \tag{7}$$

$$P^* = 1.5(V_{od}I_{od} + V_{oq}I_{oq}), \tag{8}$$

$$Q^* = 1.5(V_{od}I_{oq} - V_{oq}I_{od}), \tag{9}$$

$$\dot{P} = -\omega_{c1}P + \omega_{c1}P^*, \tag{10}$$

$$\dot{Q} = -\omega_{c2}P + \omega_{c2}Q^*. \tag{11}$$

By linearizing and rearranging the above equations, the small signal model of the DC link can be written in a state-space form as in (12):

$$\begin{aligned}\left[\Delta\dot{V}_{\text{DC}} \quad \Delta\dot{P} \quad \Delta\dot{Q}\right] = A_{ps}\left[\Delta V_{\text{DC}} \quad \Delta P \quad \Delta Q\right]^T + BP_{1s}\left[\Delta I_{idq} \quad \Delta V_{odq} \quad \Delta I_{odq}\right]^T \\ + \; BP_{2s}\Delta P_{\text{in}},\end{aligned} \tag{12}$$

where:

$$\boldsymbol{A}_{ps} = \left[\left(\frac{1}{C_{\text{DC}}V_{\text{DC}}}\right)\left[\frac{-P_{\text{in}} + P}{V_{\text{DC}}} \;\; -1 \;\; 0\right]^T \;\; [0 \;\; -\omega_{c1} \;\; 0]^T \;\; [0 \;\; 0 \;\; -\omega_{c2}]^T\right]^T,$$

$$\boldsymbol{BP}_{2s} = (1/C_{\text{DC}}V_{\text{DC}})\,[1 \;\; 0 \;\; 0]^T,$$

$$\boldsymbol{BP}_{1s} = 1.5\left[[0 \;\; 0 \;\; 0 \;\; 0 \;\; 0 \;\; 0]^T \;\; \left[0 \;\; 0 \;\; \omega_{c1}I_{od} \;\; \omega_{c1}I_{oq} \;\; \omega_{c1}V_{od} \;\; \omega_{c1}V_{oq}\right]^T \right.$$
$$\left.\left[0 \;\; 0 \;\; \omega_{c2}I_{oq} \;\; -\omega_{c2}I_{od} \;\; -\omega_{c2}V_{oq} \;\; \omega_{c2}V_{od}\right]^T\right]^T.$$

Equations (8) and (9) can be further simplified by making V_{oq} zero, and then they can be used to control the active power (P) and reactive power (Q) delivered by the converter. The dynamics of the DC link voltage can be easily controlled at the reference value (V_{DCref}) to regulate the active power delivered to the grid. Also, reactive power is regulated at fixed reference value (Q_{ref}), and corresponding dynamic equations can be constructed as listed in (13), (14), (15), and (16). Here φ_d and φ_q are variables used to represent the d and q-axis input errors. Also, I_{id}^* and I_{iq}^* are d and q-axis desired current on the inverter side.

$$Q_{\text{ref}} - Q = \dot{\varphi}_q, \tag{13}$$

$$V_{\mathrm{DC}} - V_{\mathrm{DC\,ref}} = \dot{\varphi}_d \,, \tag{14}$$

$$I_{id}^{*} = K_{po1s}(V_{\mathrm{DC}} - V_{\mathrm{DC\,ref}}) + K_{io1s}\varphi_d \,, \tag{15}$$

$$I_{iq}^{*} = K_{po2s}(Q_{\mathrm{ref}} - Q) + K_{io2s}\varphi_q \,. \tag{16}$$

By linearizing and rearranging the above equations, the small signal model of the power control block can be written in a state-space form as in (17) and (18), respectively.

$$\left[\Delta\dot{\varphi}_{dq}\right] = A_{os}\left[\Delta\varphi_{dq}\right] + B_{o1s}\left[\Delta V_{\mathrm{DC}} \;\; \Delta P \;\; \Delta Q\right]^T , \tag{17}$$

$$\left[\Delta I_{idq}^{*}\right] = C_{os}\left[\Delta\varphi_{dq}\right] + D_{o1s}\left[\Delta V_{\mathrm{DC}} \;\; \Delta P \;\; \Delta Q\right]^T , \tag{18}$$

where:

$$\begin{aligned}
\boldsymbol{A}_{os} &= \left[\left[0 \;\; 0\right]^T \;\; \left[0 \;\; 0\right]^T\right]^T , \\
\boldsymbol{B}_{o1s} &= \left[\left[1 \;\; 0 \;\; 0\right]^T \;\; \left[0 \;\; 0 \;\; -1\right]^T\right]^T , \\
\boldsymbol{C}_{os} &= \left[\left[K_{io1s} \;\; 0\right]^T \;\; \left[0 \;\; K_{io2s}\right]^T\right]^T , \\
\boldsymbol{D}_{o1s} &= \left[\left[K_{po1s} \;\; 0 \;\; 0\right]^T \;\; \left[0 \;\; 0 \;\; -K_{po2s}\right]^T\right]^T .
\end{aligned}$$

Feedback responses of voltage and current improve the stability and the transient response of the inverter current. The reference current given by the power control loop is used as the input of the current loop. Therefore, (19) and (20) defining the state space model of the current loop considers the representation defined in [16]. Here, γ_d and γ_q are variables used to represent the d and q-axis input errors.

$$\left[\Delta\dot{\gamma}_{dq}\right] = A_{Is}\left[\Delta\gamma_{dq}\right] + B_{I1s}\left[\Delta I_{idq}^{*}\right] + B_{I2s}\left[\Delta I_{idq} \;\; \Delta V_{odq} \;\; \Delta I_{odq}\right]^T , \tag{19}$$

$$\left[\Delta V_{idq}^{*}\right] = C_{Is}\left[\Delta\gamma_{dq}\right] + D_{I1s}\left[\Delta I_{idq}^{*}\right] + D_{I2s}\left[\Delta I_{idq} \;\; \Delta V_{odq} \;\; \Delta I_{odq}\right]^T . \tag{20}$$

The LC filter can filter out the second-order and other high-order harmonics generated by high-frequency switching. The state space form can represent the linearized equations of the filter equations as in (21), and it has a similar representation defined in [16].

$$\begin{aligned}
\left[\Delta\dot{I}_{idq} \;\; \Delta\dot{V}_{odq} \;\; \Delta\dot{I}_{odq}\right] = {} & A_{Ls}\left[\Delta I_{idq} \;\; \Delta V_{odq} \;\; \Delta I_{odq}\right]^T + BLC_{1s}\left[\Delta V_{id}^{*} \;\; \Delta V_{iq}^{*}\right]^T \\
& + BLC_{2s}\left[\Delta V_{bdq}\right] + BLC_{3s}\left[\Delta\omega\right] .
\end{aligned} \tag{21}$$

The voltage at the point where the inverter is connected to the grid is considered as the input to the system and subjected to the transformation in (1) and the simplification in (22). The models of the subsystems given by (12), (17), (18), (19), (20), and (21) should be interconnected to get the complete state space model of the grid following inverter shown in (23).

$$T_V^{-1} \cdot \Delta\delta = (\partial T_s^{-1}/\partial\delta) \cdot V_{DQ}, \tag{22}$$

$$\Delta\dot{x} = A_s\left[\Delta x\right] + B_s\left[\Delta V_{bdq}\right] + C_s\left[\Delta\omega_{\mathrm{com}}\right] + D_s\left[\Delta P_{\mathrm{in}}\right] , \tag{23}$$

where:

$$\boldsymbol{\Delta x} = \left[\Delta\delta \;\; \Delta P_{LL} \;\; \Delta V_{\mathrm{DC}} \;\; \Delta P \;\; \Delta Q \;\; \Delta\varphi \;\; \Delta\gamma \;\; \Delta I_{idq} \;\; \Delta V_{odq} \;\; \Delta I_{odq}\right]^T ,$$

$$\boldsymbol{A}_s = \begin{bmatrix} A_{PLLs} & 0 & 0 & 0 & B_{2PLLs} \\ 0 & A_{ps} & 0 & 0 & B_{p1s} \\ 0 & B_{o1s} & A_{os} & 0 & 0 \\ 0 & B_{I1s}\cdot D_{o1s} & B_{I1s}\cdot C_{os} & A_{Is} & B_{I2s} \\ \begin{pmatrix} BLC_{3s}\cdot C_{PLLs} \\ +BLC_{2s}[T_v^{-1}\ 0] \end{pmatrix} & \begin{pmatrix} BLC_{1s} \\ \cdot D_{I1s}\cdot D_{os} \end{pmatrix} & \begin{pmatrix} BLC_{1s} \\ \cdot D_{I1s}\cdot C_{os} \end{pmatrix} & BLC_1\cdot C_{Is} & \begin{pmatrix} A_{Ls} \\ +BLC_{1s}\cdot D_{I2s} \\ +BLC_{3s}\cdot D_{PLLs} \end{pmatrix} \end{bmatrix},$$

$$\boldsymbol{B}_s = \left[0\ 0\ 0\ BLC_{2s}\cdot T_s^{-1}\right]^T, \quad \boldsymbol{C}_s = [B_{1PLLs}\ 0\ 0]^T, \quad \boldsymbol{D}_s = [0\ Bp2s\ 0\ 0]^T.$$

3.2. Energy storage

The energy storage system operates in the grid-forming mode during the islanded operation and the grid following mode during the grid-connected operation. A bidirectional buck-boost converter and associated control facilitate the charging and discharging process [31]. Based on the assumption: energy storage being an ideal source, the DC bus dynamics are neglected, and the inverter dynamics are also neglected with the realization of high switching frequencies. Therefore, the state space model of the energy storage is derived considering the dynamics of the inverter.

Therefore, the final state space model takes the representations given in (24) and (25). It is similar to general state space modeling of grid forming converters. More details on the state space modeling of grid-forming converters can be found in [16]. Here, m_p and ω are (P–f) droop coefficient and output frequency set by the converter, respectively.

$$\Delta\dot{x} = A_b\left[x\right] + B_b\left[\Delta V_{bdq}\right] + C_b\left[\Delta\omega_{\text{com}}\right], \tag{24}$$

$$\Delta\omega = C_{\text{invc}}\cdot\Delta x, \tag{25}$$

where:

$$\boldsymbol{\Delta x} = \left[\Delta\delta\ \Delta P\ \Delta Q\ \Delta\varphi\ \Delta\gamma\ \Delta I_{idq}\ \Delta V_{odq}\ \Delta I_{odq}\right]^T, \quad \boldsymbol{C}_{\textbf{invc}} = [0\ -mp\ 0\,0\,0\,0\,0\,0\,0\,0\,0\,0\,0].$$

3.3. Diesel generator

The synchronous generator-based diesel generator, i.e., Genset, consists of a prime-mover (the engine) driving a synchronous machine through a mechanical shaft. A generator excitation system regulates its terminal voltage, and frequency is controlled through the engine speed governor if it is in droop mode [14]. If the unit operates in the PQ control mode, the reference power to the governor is set based on the desired output active power [32]. Considering the slow response of the governor and the time constants associated with the excitation control system, the dynamics of the active and reactive power control were neglected, considering the fast response of the rotor angle [26]. Therefore, the state space model of the diesel generator was represented by the dynamics of the synchronous machine only.

According to [26], the state space equation illustrated in (26) can be obtained by developing the dynamic equations for the stator, field winding, damping windings of a general model of a synchronous machine, and linearizing around a steady point. Here, V_a and I_a are the voltage and the current of the winding denoted by the subscript (d and q for stator winding, F for field

winding, DD and QQ for damper winding). Also, T is the mechanical torque of the generator.

$$\Delta v = -k\Delta x - M\Delta\dot{x}, \tag{26}$$

where:

$$\boldsymbol{\Delta v} = \left[\Delta V_d\ \Delta V_q\ \Delta V_F\ \Delta V_{DD}\ \Delta V_{QQ}\ \Delta T\ \Delta\omega_{\text{com}}\right]^T, \quad \boldsymbol{\Delta x} = \left[\Delta i_d\ \Delta i_q\ \Delta i_F\ \Delta i_{DD}\ \Delta i_{QQ}\ \Delta\omega_r\ \Delta\delta\right]^T.$$

Also, the voltage at the point where the generator is connected to the grid is considered as the input to the system, and it should be subjected to the transformation in (1) if necessary. Here, k and M are (7×7) matrices, and their detailed representation can be found in general synchronous machine modelling as presented in [26]. Equation (26) can be further simplified and can be expressed as in (27).

$$\Delta\dot{x} = A_g\Delta x + B_g\Delta V_{dq} + C_g\Delta T + D_g\Delta\omega_{\text{com}} + E_g\left[\Delta V_F \quad \Delta V_{DD} \quad \Delta V_{QQ}\right]^T, \tag{27}$$

where $\boldsymbol{A}_g = -M^{-1}k$, and $\boldsymbol{B}_g$, $\boldsymbol{C}_g$, $\boldsymbol{D}_g$ and $\boldsymbol{E}_g$ correspond to elements in $-M^{-1}$.

3.4. Dynamic load

In stability studies of microgrids, the dynamics associated with the induction motors are an important aspect of the dynamic characteristics of the system loads [33]. Even if the modelling of the synchronous generator was done considering a reference frame rotating with the rotor, the reference frame for induction motor modelling is considered as the one rotates at the common system frequency. The d-axis is assumed to be 90°ahead of the q-axis in the direction of rotation. The stator (subscript, s) and rotor (subscript, r) voltage can be derived in terms of the d and q-components as illustrated in (28), (29), (30), and (31), respectively [33]. Here, v_a is the flux linking the winding denoted by the corresponding subscript. R_s and R_r are stator and rotor per phase resistance, respectively. Also, ω_s and ω_r are the common system frequency and speed of the rotor respectively, while p representing a differential operator, $\frac{\mathrm{d}}{\mathrm{d}t}$, and $P\theta_r$ representing the difference between ω_s and ω_r.

$$V_{ds} = R_s i_{ds} + \omega_s(L_{ss}i_{qs} + L_m i_{qr}) + p(L_{ss}i_{ds} + L_m i_{dr}), \tag{28}$$

$$V_{qs} = R_s i_{qs} - \omega_s(L_{ss}i_{ds} + L_m i_{dr}) + p(L_{ss}i_{qs} + L_m i_{qr}), \tag{29}$$

$$V_{dr} = R_r i_{dr} + (p\theta_r)(L_{rr}i_{qr} + L_m i_{qs}) + p(L_{rr}i_{dr} + L_m i_{ds}), \tag{30}$$

$$V_{qr} = R_r i_{qr} - (p\theta_r)(L_{rr}i_{dr} + L_m i_{ds}) + p(L_{rr}i_{qr} + L_m i_{qs}), \tag{31}$$

where: L_{rr} is the difference between the self-inductance of rotor winding and the mutual inductance of rotor windings; L_{ss} is the difference between the self-inductance of the stator winding and mutual inductance of stator windings; L_m is magnetizing inductance.

By linearizing and rearranging the dynamic equations illustrated by (28), (29), (30), and (31), matrix form and the state space model shown by (32) and (33) can be obtained. Here, rotor voltages are zero as the rotor winding are short-circuited.

$$A_1\left[\Delta\dot{i}_{ds} \quad \Delta\dot{i}_{qs} \quad \Delta\dot{i}_{dr} \quad \Delta\dot{i}_{qr}\right]^T = B_1\left[\Delta i_{ds} \quad \Delta i_{qs} \quad \Delta i_{dr} \quad \Delta i_{qr}\right]^T + B_2\Delta\omega_r + B_3\Delta\omega_s + B_4\left[\Delta v_{ds} \quad \Delta v_{qs}\right]^T, \tag{32}$$

where:

$$\boldsymbol{A}_1 = \begin{bmatrix} L_{ss} & 0 & L_m & 0 \\ 0 & L_{ss} & 0 & L_m \\ L_m & 0 & L_{rr} & 0 \\ 0 & L_m & 0 & L_{rr} \end{bmatrix},$$

$$\boldsymbol{B}_1 = \begin{bmatrix} -R_s & -\omega_s L_{ss} & 0 & -\omega_s L_m \\ \omega L_{ss} & -R_s & \omega_s L_m & 0 \\ 0 & -(\omega_s - \omega_r) L_m & -R_r & -(\omega_s - \omega_r) L_{rr} \\ (\omega_s - \omega_r) L_m & 0 & (\omega_s - \omega_r) L_{rr} & -R_r \end{bmatrix},$$

$$\boldsymbol{B}_2 = \begin{bmatrix} 0 & 0 & L_{rr} i_{qr} + L_m i_{qs} & -L_{rr} i_{dr} & -L_m i_{ds} \end{bmatrix}^T,$$

$$\boldsymbol{B}_3 = \begin{bmatrix} -L_{ss} i_{qs} & -L_m i_{qr} \\ L_{ss} i_{ds} & +L_m i_{dr} \\ -L_{rr} i_{qr} & -L_m i_{qs} \\ L_{rr} i_{dr} & +L_m i_{ds} \end{bmatrix}^T,$$

$$\boldsymbol{B}_4 = \begin{bmatrix} \begin{bmatrix} 1 & 0 & 0 & 0 \end{bmatrix}^T & \begin{bmatrix} 0 & 1 & 0 & 0 \end{bmatrix}^T \end{bmatrix},$$

$$\Delta \dot{x} = A^{-1} B_1 \Delta x + A^{-1} B_2 \Delta \omega_r + A^{-1} B_3 \Delta \omega + A^{-1} B_4 \Delta v_{dq} \,. \tag{33}$$

The electromagnetic torque drives the mechanical load connected to the rotor, and the mismatch between the mechanical (T_m) and electrical (T_e) torque governs the rate of change in the speed of rotor mass. Therefore, (34) defines the torque mismatch and the rate of change in rotor speed (ω_r). Here, B and H are the damping constant and inertia constant, respectively.

$$\dot{\omega}_r 2H = (T_e/3) - T_m - B\omega_r \,. \tag{34}$$

Writing the electromagnetic torque (T_e) in terms of stator and rotor currents [33], and substituting to (34), the state space model shown by (34) can be obtained by linearizing. Here, $J = 2H$, and electromagnetic torque (T_e) should be divided by three as shown in (34), if per unit torque base is defined on per phase base.

$$\Delta \dot{\omega}_r = C_1 \begin{bmatrix} \Delta i_{ds} & \Delta i_{qs} & \Delta i_{dr} & \Delta i_{qr} \end{bmatrix}^T + C_2 \Delta \omega_r - (1/J) \Delta T_m \,, \tag{35}$$

where:

$$\boldsymbol{C}_1 = (1.5/3J) \begin{bmatrix} L_m i_{qr} & -L_m i_{dr} & -L_m i_{qs} & L_m i_{ds} \end{bmatrix}, \qquad \boldsymbol{C}_2 = [-B/J] \,.$$

Models of the mechanical system and windings of the motor should be interconnected to get the complete state space model of three phase induction motor. Therefore, the final state space model takes the representation given in (36). If the induction motor is a two-pole machine, then synchronous speed and common system frequency are the same. Therefore, if necessary, it should be subjected to the transformation in (1).

$$\Delta \dot{x} = A \Delta x + B \Delta \omega_{\text{com}} + C \Delta v_{sdq} + D \Delta T_m \,, \tag{36}$$

where:

$$\begin{aligned}
\boldsymbol{\Delta x} &= \begin{bmatrix} \Delta i_{dqs} & \Delta i_{dqr} & \Delta\omega_r \end{bmatrix}^T, \\
\boldsymbol{A} &= \begin{bmatrix} \begin{bmatrix} A_1^{-1}B_1 & A_1^{-1}B_2 \end{bmatrix} & \begin{bmatrix} C_1 & C_2 \end{bmatrix} \end{bmatrix}^T, \\
\boldsymbol{B} &= \begin{bmatrix} A_1^{-1}B_3 & 0 \end{bmatrix}^T, \\
\boldsymbol{C} &= \begin{bmatrix} A_1^{-1}B_4 & 0 \end{bmatrix}^T, \\
\boldsymbol{D} &= \begin{bmatrix} 0 & 0 & -1/J \end{bmatrix}^T.
\end{aligned}$$

3.5. Network

The dynamics of the static loads and the cable network can be neglected considering the fast response relative to the DERs and dynamic loads. Therefore, an impedance-based system can adequately represent them, and a corresponding admittance matrix can be derived by incorporating the static loads in terms of constant impedance loads [14]. Equivalent π-models are used to represent the cables. The buses with zero current can be eliminated from the admittance matrix via Kron reduction [34]. After the reduction, the admittance matrix in phase-based form as in (37) can be derived, and the admittance matrix is transformed to a new modified matrix in the *dq* framework as in (38) and (39). Note that state variables of the network have been defined on the common reference frame.

$$[\Delta I] = Y\,[\Delta V]\,, \tag{37}$$

$$\begin{bmatrix} I_{d1}\, I_{q1}\, I_{d2}\, I_{q2}\, \cdots\, I_{qn} \end{bmatrix}^T = \begin{bmatrix} \mathrm{Real}(Y_{11}) & \mathrm{Img}(Y_{11}) & \cdots & \mathrm{Img}(Y_{1n}) \\ -\mathrm{Img}(Y_{11}) & \mathrm{Real}(Y_{11}) & \cdots & \mathrm{Real}(Y_{1n}) \\ \vdots & \vdots & \ddots & \vdots \\ -\mathrm{Img}(Y_{n1}) & \cdots & \cdots & \mathrm{Real}(Y_{nn}) \end{bmatrix} \begin{bmatrix} V_{d1}\, V_{q1}\, V_{q2}\, \cdots\, V_{qn} \end{bmatrix}^T, \tag{38}$$

$$\begin{bmatrix} \Delta V_{DQ} \end{bmatrix} = Y^{-1} \begin{bmatrix} \Delta I_{DQ} \end{bmatrix}. \tag{39}$$

The current vector defined on the common reference frame can be written as a summation of the current injected by DERs at each bus bar. Also, the transformation of current states explained by (2) can be redefined as illustrated in (40) to map the current states at each bus bar defined on the individual reference frame of each DER to the common reference frame. Equation (41) illustrates how the current injected by a grid-following converter can be written in terms of the state vector of the particular grid-following converter. Therefore, the current at each bus bar defined in the modified admittance matrix can be written in terms of state vectors corresponding to the DERs connected to the particular bus as illustrated in (42), and it can be expanded to represent the whole bus network as represented by (43). Here, $\boldsymbol{C}_{\mathrm{mot}}$ and $\boldsymbol{C}_{\mathrm{gen}}$ are diagonal matrices, and $\boldsymbol{C}_{\mathrm{mot}i}$ and $\boldsymbol{C}_{\mathrm{gen}i}$ corresponds to the diagonal elements. Also, $\boldsymbol{C}_{\mathrm{inv}}$ is a combination of two diagonal matrices corresponding to the grid forming converters and grid following converters. State vectors of the grid forming and following converters have been combined into a single state vector.

$$\Delta I_{oDQi} = T_{Vi}\Delta\delta + T_{Si} \cdot \Delta I_{odqi}\,, \tag{40}$$

where:

$$T_{vi} \cdot \Delta\delta = \frac{\partial T_{Si}}{\partial \delta} \cdot I_{odqi},$$

$$\Delta I_{oDQi} = C_{\text{invs}i} \cdot \left[\Delta x_{\text{invs}i}\right], \tag{41}$$

where:

$$\boldsymbol{C}_{\text{invs}i} = \left[T_{Vi}\ 0\ 0\ 0\ 0\ 0\ 0\ 0\ 0\ 0\ 0\ 0\ T_{Si}\right],$$

$$\left[\Delta V_{bDQi}\right] = \left[Y^{-1}\right]_{i\times n}\left[C_{\text{invs}i} \cdot \Delta x_{\text{invs}i} + C_{\text{inv}bi} \cdot \Delta x_{\text{inv}bi} + C_{\text{mot}i} \cdot \Delta x_{\text{mot}} + C_{\text{gen}i} \cdot \Delta x_{\text{gen}i}\right], \tag{42}$$

$$\left[\Delta V_{bDQ}\right] = Y^{-1}(C_{\text{inv}}\Delta x_{\text{inv}} + C_{\text{mot}}\Delta x_{\text{mot}} + C_{\text{gen}}\Delta x_{\text{gen}}). \tag{43}$$

3.6. Complete small signal model

Transformers can be represented as an equivalent series reactance, and voltage and current transformation ratios can be added to the state space model of individual DER if necessary.

To get the overall state space model of a generalized microgrid, as shown in Fig. 4, (23), (24), (27), and (36) defined to model a single DER should be expanded to represent all the DERs connected to the microgrid.

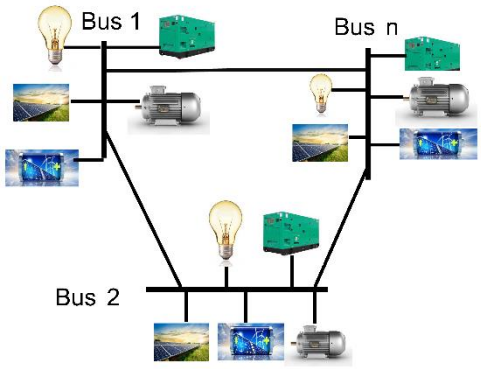

Fig. 4. Microgrid with n number of buses

State vectors of grid-forming inverters and grid-following inverters can be considered as two sets of vectors, and the state space model of all inverters can be represented as in (44). Here, it should be noted that one of the grid-forming inverters should be considered as the reference converter and its output frequency is considered as the common frequency. Therefore, $\boldsymbol{C}_{\text{inv}c}$ corresponds to the reference converter, and it is expanded with more zero elements to be equal the size of $\Delta \boldsymbol{x}_{\text{inv}}$.

$$\Delta \dot{x}_{\text{inv}} = A_{\text{inv}}\Delta x_{\text{inv}} + B_{\text{inv}}\Delta V_{bDQ} + C_{\text{inv}}P_{\text{in}}, \tag{44}$$

where:

$$\boldsymbol{A}_{\text{inv}} = \begin{bmatrix} A_{b1} + C_{b1} \cdot C_{\text{invc}} & 0 & 0 & \cdots & 0 \\ C_{b2} \cdot C_{\text{invc}} & A_{b2} & 0 & \cdots & 0 \\ \vdots & \vdots & \vdots & \ddots & \vdots \\ C_{s(n-1)} \cdot C_{\text{invc}} & 0 & 0 & A_{s(n-1)} & 0 \\ C_{sn} \cdot C_{\text{invc}} & 0 & 0 & \cdots & A_{sn} \end{bmatrix},$$

$$\boldsymbol{B}_{\text{inv}} = \begin{bmatrix} B_{b1} & 0 & 0 & \cdots & 0 \\ 0 & B_{b2} & 0 & \cdots & 0 \\ \vdots & \vdots & \vdots & \ddots & \vdots \\ 0 & 0 & 0 & B_{s(n-1)} & 0 \\ 0 & 0 & 0 & \cdots & B_{sn} \end{bmatrix}, \quad \boldsymbol{C}_{\text{inv}} = \begin{bmatrix} B_{b1} & 0 & 0 & \cdots & 0 \\ \vdots & 0 & 0 & \ddots & 0 \\ D_{s1} & 0 & 0 & 0 & 0 \\ 0 & 0 & \ddots & \ddots & 0 \\ 0 & 0 & 0 & \cdots & D_{sn} \end{bmatrix}.$$

The state space model of all generators and motors can be represented by (45) and (46), respectively. Here, $\boldsymbol{A}_{\text{gen}}$, $\boldsymbol{B}_{\text{gen}}$, $\boldsymbol{C}_{\text{gen}}$, $\boldsymbol{E}_{\text{gen}}$, $\boldsymbol{A}_{\text{motor}}$, $\boldsymbol{C}_{\text{motor}}$ are diagonal matrices. Also, diagonal values in each matrix represent the corresponding matrix of the individual motor or generator. Also, $\boldsymbol{D}_{\text{gen}}$ and $\boldsymbol{B}_{\text{motor}}$ are single column matrices having the elements in the corresponding matrix of the individual generator or motor. The complete state space model is obtained by combining the individual subsystem models given by (43), (44), (45), (46) and can be illustrated as in (47). Here, $\mathbf{Y}_1 = Y^{-1}\left[C_{\text{inv}}\right]$, $\mathbf{Y}_2 = Y^{-1}\left[C_{\text{mot}}\right]$, $\mathbf{Y}_3 = Y^{-1}\left[C_{\text{gen}}\right]$.

$$\Delta\dot{x}_{\text{gen}} = A_{\text{gen}}\Delta x_{\text{gen}} + B_{\text{gen}}\Delta V_{DQ} + C_{\text{gen}}\Delta T_m + D_{\text{gen}}\Delta\omega_{\text{com}} + E_{\text{gen}}\left[\Delta V_F \;\; \Delta V_{DD} \;\; \Delta V_{QQ}\right]^T, \quad (45)$$

$$\Delta\dot{x}_{\text{motor}} = A_{\text{motor}}\Delta x_{\text{motor}} + B_{\text{motor}}\Delta\omega_{\text{com}} + C_{\text{motor}}\Delta v_{sDQ} + D_{\text{motor}}\Delta T_m, \quad (46)$$

$$\Delta\dot{x} = A_{\text{final}}\Delta x + B_{\text{final}}\left[\Delta P_{\text{in}} \;\; \Delta T_m\right]^T + C_{\text{final}}\left[\Delta T\right] + D_{\text{final}}\left[\Delta V_F \;\; \Delta V_{DD} \;\; \Delta V_{QQ}\right]^T, \quad (47)$$

where:

$$\boldsymbol{\Delta x} = \left[\Delta x_{\text{inv}} \;\; \Delta x_{\text{mot}} \;\; \Delta x_{\text{gen}}\right]^T,$$

$$\boldsymbol{A}_{\text{final}} = \begin{bmatrix} A_{\text{inv}} + B_{\text{inv}} \cdot Y_1 & B_{\text{inv}} \cdot Y_2 & B_{\text{inv}} \cdot Y_3 \\ B_{\text{mot}} \cdot C_{\text{invc}} + C_{\text{mot}} \cdot Y_1 & A_{\text{mot}} + C_{\text{mot}} \cdot Y_2 & C_{\text{mot}} \cdot Y_3 \\ D_{\text{gen}} \cdot C_{\text{invc}} + B_{\text{gen}} \cdot Y_1 & B_{\text{gen}} \cdot Y_2 & A_{\text{gen}} + B_{\text{gen}} \cdot Y_3 \end{bmatrix},$$

$$\boldsymbol{B}_{\text{final}} = \left[\left[C_{\text{inv}} \;\; 0\right]^T \;\; \left[0 \;\; D_{\text{mot}}\right]^T \;\; \left[0 \;\; 0\right]^T\right]^T,$$

$$\boldsymbol{C}_{\text{final}} = \left[0 \;\; 0 \;\; C_{\text{gen}}\right]^T,$$

$$\boldsymbol{D}_{\text{final}} = \left[0 \;\; 0 \;\; E_{\text{gen}}\right]^T.$$

4. Validation of small signal model

The microgrid model shown in Fig. 1(a) was used to validate the small signal model. Steady-state values of DERs and loads listed in Table 1 were extracted via load flow analysis, using PSS/E University edition. Both the state space model and transient simulation model were subjected to step changes, and resultant transient waveforms are compared. The PSCAD/EMTDC v4.6.3

software was used for transient simulation, and MATLAB R2020a was used to model the state space equations and get the corresponding curves.

Table 1. Power flow at a steady state condition

Load/DER	**Active power (kW)**	**Reactive power (kvar)**
Static load 1	272	137
Static load 2	1 452	734
Dynamic load 1	35	13.2
Dynamic load 2	160	67
Generator	493	0
Solar	2 500	0
Energy storage	–1 070.3	966

Figure 5 shows the variation of the d-axis and q-axis stator current drawn by the motor after a step change in dynamic load 2.

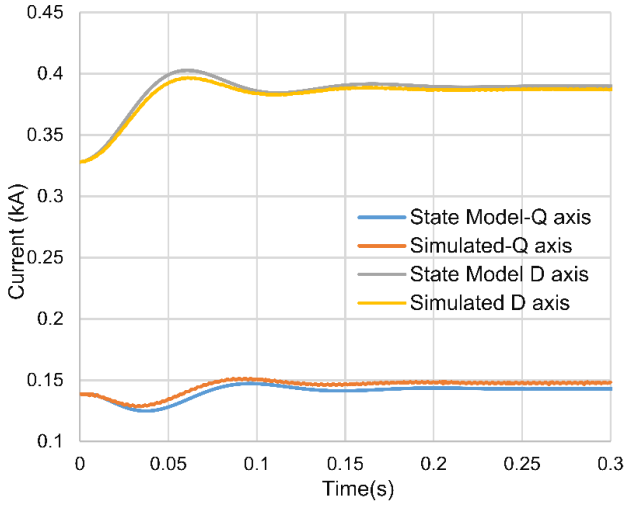

Fig. 5. Transient of d and q-axis current of the dynamic load 2 upon a step change

The transient curves given by the state space model and simulation models are almost the same. However, the resultant current transient at the terminal of energy storage is not visible due to a small change in power drawn from the energy storage. Therefore, the corresponding waveform is not presented in this article.

The transient curve of the stator q-axis current and the corresponding transient of the active power at the terminal of the energy storage during a step change of mechanical torques of the

generator are shown in Fig. 6(a), and Fig. 6(b), respectively. Transient and change of the stator d-axis current is almost negligible and therefore the corresponding curve is not presented. The q-axis curves given by the simulated model and the state space model look the same, with a small offset. The state space model of the generator was developed, neglecting the effect of the excitation system and governor for a short period because time constants associated with the excitation system and governor are higher than those associated with the dynamics of the rotor [26]. However, in the transient simulation model, the effect of the excitation system and time lag associated with the diesel engine comes into action. It is reflected by the current offsets and time lag between the curves given by the simulation and state space models.

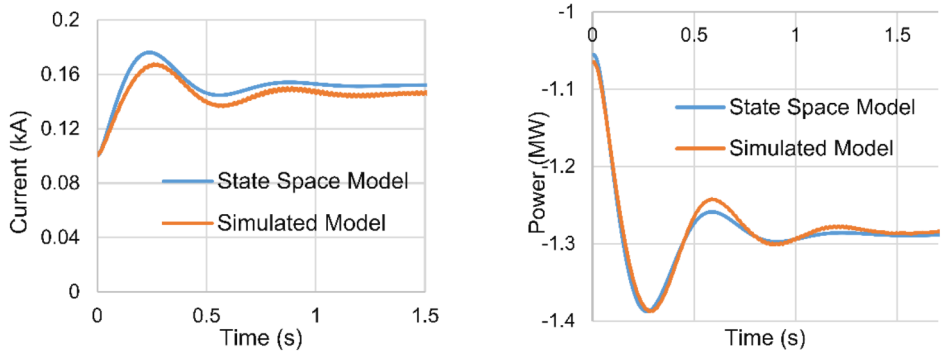

(a) (b)

Fig. 6. Transients upon a step change of mechanical torques of the generator: transient of q-axis stator current (a); transient of active power at the terminal of energy storage (b)

A step change in the output power of the solar panels results in transients of the active power at the terminal of the solar PV system under two different outer loop controller gains ($K_{po1s} = K_{po2s} = 0.05$ and $K_{po1s} = K_{po2s} = 0.005$), as illustrated in Fig. 7(a), and Fig. 7(b),

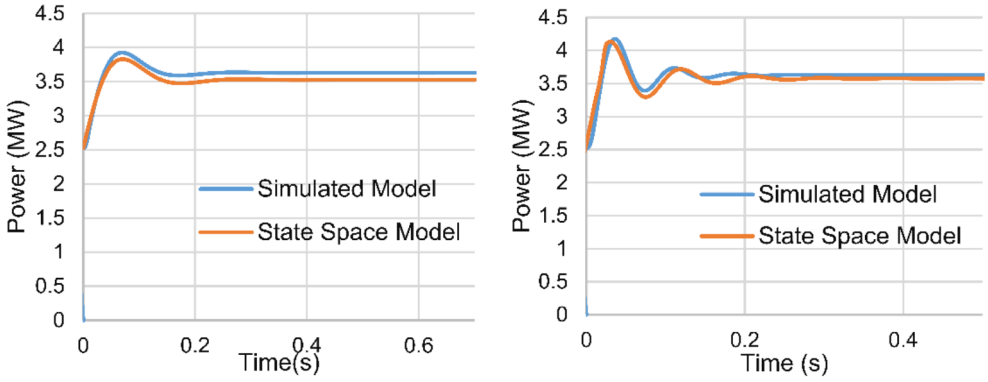

(a) (b)

Fig. 7. Transients power at the terminal of the solar PV system upon a step change of output power of solar panel: $K_{pos} = 0.05$ (a); $K_{pos} = 0.005$ (b)

respectively. It should be noted that in this study, two proportional gains in each control loop of the DERs are tuned to have the same values. Also, each integral gain is tuned in the same way. The shape of the transient is almost the same with a slight offset between the two curves given by the simulated model and the state space model. The deviation is due to an offset error associated with the dynamics of the boost converter in the rooftop solar PV system. It is reflected in the simulation results since the dynamics of the boost converter are not considered during the development of the state space model.

The curves given by the state-space models are in a good agreement with the waveforms given by the simulation model producing the same transient and steady-state values with the same progression in time in most cases. Therefore, the accuracy of the developed small-signal model is satisfactorily validated.

5. Robustness of microgrids with small disturbances

A microgrid is delivering energy from various energy sources with the help of power electronic converters. Also, power electronics interfaces offer flexible control strategies. However, the stability of the microgrid in the islanded operation can be easily affected by the issues in local controls [14]. Small perturbations caused by small load changes, system damping, and mismatches in feedback controllers can cause local oscillations with the interaction of control systems [22].

Therefore, a small signal analysis is conducted to make sure the designed microgrid is stable with small disturbances under all operating scenarios. The microgrid is subjected to the 24-hour load profile, generating 24 cases for analysis. The state matrix for each case is calculated by taking steady-state points via load flow analysis. The small signal state models of dynamic load, synchronous machine, energy storage, and solar PV system have five, seven, thirteen, and fifteen state variables, respectively. Therefore, there will be 45 state variables in the case study. With a high-performance PC with an Intel i7 processor, the total time taken by MATLAB was around 5 minutes. The eigenvalues are calculated for the microgrid shown in Fig. 1(a). Accordingly, Fig. 8(a) illustrates the distribution of all 1080 eigenvalues in the real and imaginary coordinate system for the considered system load scenario for a 24-hour period.

All the eigenvalues are located on the negative plane implying a stable microgrid irrespective of the load profile. Also, two eigenvalues are travelling with the 24 hours' load, as illustrated in Fig. 8(a) (inside the ellipse). Other eigenvalues with the same index corresponding to a particular load profile coincide with each other.

Therefore, all the eigenvalues (except travelling eigenvalues) with the same index cannot be clearly observable in real and imaginary planes. Travelling eigenvalues were further analyzed because of their possibility to travel toward the zero axis and jump to the positive plane, which can make the system unstable.

In the participation factor analysis, states with participation lower than 1% are not considered. Figure 8(b) shows the participation of the state variable on mode 1 and mode 2 (two travelling eigenvalues).

Here, subscripts s, b, and G correspond to states associated with the solar PV system, battery storage, and diesel generator. There are four effective state variables contributing to the travelling

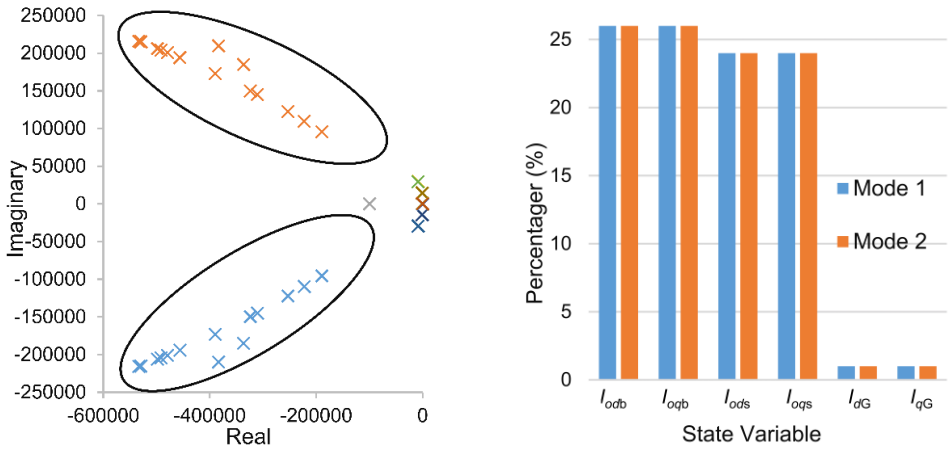

(a) (b)

Fig. 8. Distribution of eigenvalues and details of travelling eigenvalues: distribution of eigenvalues (a); participation in the travelling eigenvalues (b)

eigenvalues except for the d and q-axis stator current contribution of the generator around 1%. Since modes 1 and 2 are related to two conjugate eigenvalue pairs, the contribution of the d and q-axis states of the same electrical quantities on a particular mode is the same. Grid side d and q-axis current of the grid forming and following converters contributes to mode 1 and mode 2 by around 25%.

The damping ratio defines the decay rate of the amplitude of the oscillation states. Modes with a low damping ratio can lead to longer oscillations in the system. The interaction of the oscillatory event might lead to more oscillatory conditions, resulting in deterioration of system damping or even unstable situations [33]. In this article, the modes with lower damping ratios below 20% and lower damping frequencies are subjected to the participation factor analysis. There are six such critical modes, as listed in Table 2.

Table 2. Modes with low damping ratios

Mode	Eigenvalue	Damping ratio (%)	Damping frequency (rad/s)	Natural frequency (rad/s)
8	–1292+14504i	8.87	2 309	2 318
9	–1292–14504i	8.87	2 309	2 318
10	–1453+14348i	10.0	2 284	2 296
11	–1453–14348i	10.0	2 284	2 296
22	–7+318i	2.2	50	50
23	–7–318i	2.2	50	50

Fig. 9 shows the participation of the state variable on modes 8–11, 22 and 23.

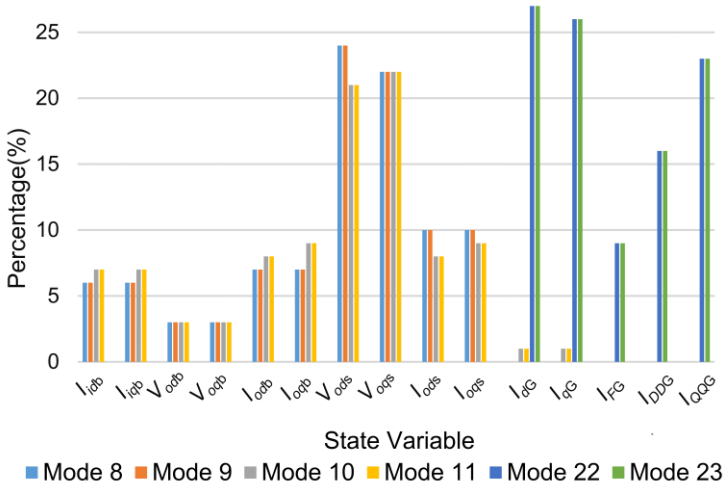

Fig. 9. Participation of the state variable on the modes

Here, subscripts *s*, *b*, and *G* correspond to states associated with the solar PV system, battery storage, and diesel generator. The eigenvalues associated with lower damping ratios are contributed by the states of the stator and rotor current of the diesel generator. The *d* and *q*-axis stator current contribute to modes 22 and 23 by more than 25%.

The microgrid includes an energy management system to handle all possible power-sharing scenarios. Trajectories of critical modes and travelling modes are considered under five solar PV penetration levels of 100%, 82%, 45%, 19%, and 0% while maintaining the same load profile as listed in Table 3 to study the effect of solar PV penetration on small signal stability of the microgrid. Furthermore, the diesel generator is permitted to operate at a minimum load of 30% of its nominal rating. Figure 10 depicts eigenvalue trajectories at various solar penetration levels. Eigenvalues corresponding to a particular mode coincide with each other and there is no movement with the level of solar PV penetration. When compared to small signal stability studies

Table 3. The power profile of the microgrid under different solar penetration levels

Load (kW)	**Solar PV (kW)**	**Battery (kW)**	**Generator (kW)**
1 741	3 121	–2 039	660
1 741	2 724	–1 642	660
1 741	1 409	–2 069	660
1 741	603	478	660
1 741	0	1 081	660

on microgrids with decentralized energy management systems [19], it is discovered that the level of solar PV penetration has no significant effect on the critical modes and the travelling modes when the inverter is operated on the grid following mode. Thus, as a result of the impedance changes in the distribution network caused by different load conditions, mode 1 and mode 2 travelled in Fig. 8(a).

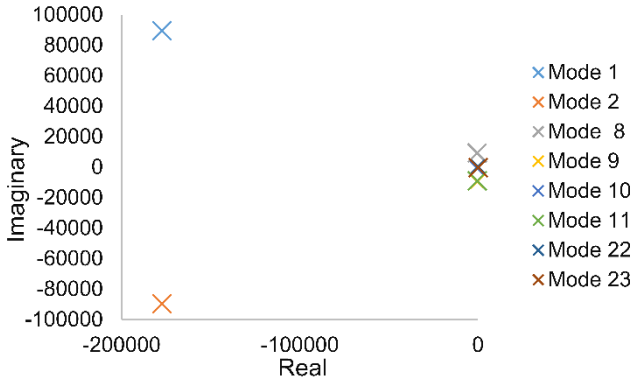

Fig. 10. Distribution of critical eigenvalues with different solar penetration

The gain parameters, line impedances, and loads all have an impact on the dynamic behavior and stability of microgrids [19]. Line parameters, on the other hand, can be considered constant according to the primary design. Furthermore, for the considered load conditions, the travelling eigenvalues do not cross the imaginary axis and are not associated with critical damping ratios. Therefore, the effect of the significant tunable parameters on the critical damping ratios of the investigated microgrid is taken into account in this article to increase the stability of the microgrid.

According to the participation factor analysis of critical modes depicted in Fig. 9, critical eigenvalues are primarily derived from states associated with the inverters. This study presents critical mode trajectory variations with gain control parameters of the two inverters. In certain ranges, a small variation in the proportional and integral gain of the converters in solar PV systems and battery storage is considered, as shown in Table 4. Here, K_{pob} and K_{iob} are the proportional and integral gain of the voltage loop of the battery storage while the K_{pib} and K_{iib} are the proportional and integral gain of the current loop of the battery storage. Also, $K_{pos}(K_{po1s} = K_{po2s} = K_{pos})$ and $K_{ios}(K_{io1s} = K_{io2s} = K_{ios})$ are the proportional and integral time gain of the power loop of the solar PV system while the K_{pis} and K_{iis} are the proportional and integral gain of the current loop of the battery storages.

Table 4. Variation of considered control gains

Control gain	K_{pob}	K_{iob}	K_{pib}	K_{iib}	K_{pos}	K_{ios}	K_{pis}	K_{iis}
Range	1.18–2.17	563–763	23–43	2212–2612	1.03–2.03	186–386	1.97–21.97	1205–1605

Figures 11(a)–11(f) illustrate the trajectory of critical modes listed in Table 2, on the real and imaginary coordinate system upon the variation of the gain parameters listed in Table 4. As the proportional gain (K_{pob}) of the battery's voltage loop is increased from 1.18 to 2.17, modes 8–10, and 11 move toward the imaginary axis as in Fig. 11(a), implying a deterioration in dynamic response. Even though modes 22 and 23 initially do not move, instantly damping ratios change their value from 2.2% to 100% and begin moving to the left as shown in Fig. 11(a). The

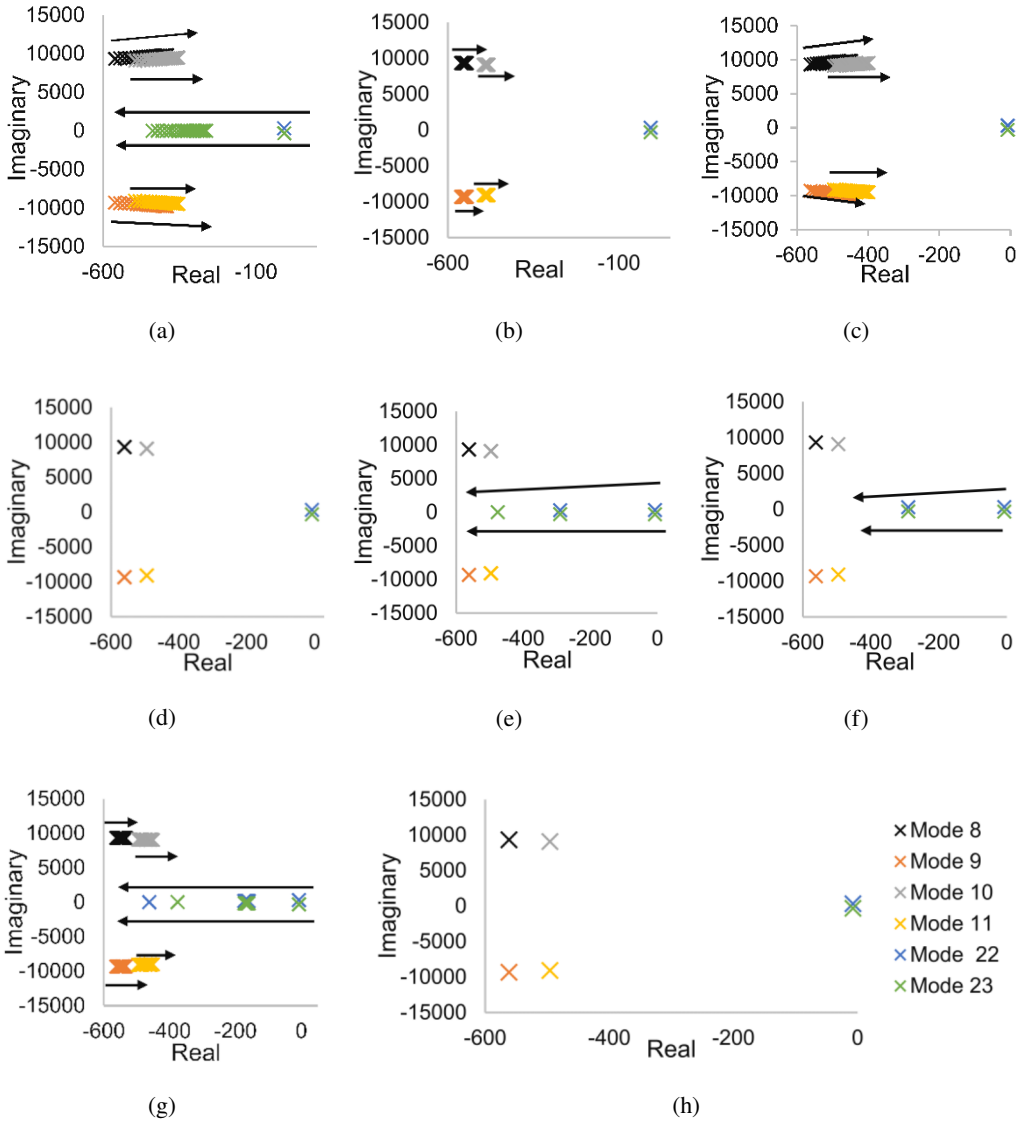

Fig. 11. Trajectories of critical modes under the variation of the gains of the controllers: K_{pob} (a); K_{iob} (b); K_{pib} (c); K_{iib} (d); K_{pos} (e); K_{ios} (f); K_{pis} (g); K_{iis} (h)

changes in the K_{pob} value affect the system's dynamic behavior, and the state variable associated with the generator is no longer participating in modes 22 and 23.

The increase in the integral gain (K_{iob}) of the voltage loop from 563 to 763, on the other hand, has only a minor effect on the trajectories of modes 8, 9, 10, and 11 as illustrated in Fig. 11(b) moving towards the imaginary axis. However, the effect on modes 22 and 23 is insignificant. Trajectories of critical modes show similar behaviour as in the voltage loop when the proportional gain (K_{pib}) of the current loop of the battery storage is increased from 23 to 43 as illustrated in Fig. 11(c). The increase in the integral time constant (K_{iib}) value from 2212 to 2612, on the other hand, does not affect the trajectories of all modes as illustrated in Fig. 11(d).

As the proportional gain (K_{pos}) and integral gain (K_{ios}) of the solar PV system's power loop are increased from 1.03 to 2.03, and from 186 to 386, all modes initially do not move as shown in Fig. 11(e) and Fig. 11(f). Modes 22 and 23 exhibit damping ratio enhancement as they move to the left while changing the damping value to 100% from 2.2% at high K_{pos} and K_{ios} values, whereas modes 8–10, and 11 are unaffected by control gains. Modes 8–10, and 11 move slightly toward the imaginary axis as the proportional gain (K_{pis}) of the solar PV system's current loop increases as shown in Fig. 11(g), whereas modes 22 and 23 do not. However, they suddenly improve their damping ratio from 2.2% to 100%. However, the integral gain (K_{iis}) of the solar PV system's current loop does not affect all modes as shown in Fig. 11(h).

The analysis of gain parameters on critical modes reveals that modes 8–10, and 11 move towards the positive plane upon a slight increase in their value, reducing system stability. Furthermore, the inverter control gain parameters do not affect modes 22 and 23. However, at high gain values, the generator no longer participates in modes 22 and 23, and therefore modes 22 and 23 suddenly achieve a damping ratio of 100% while moving away from the zero axis.

6. Conclusions

This paper presented a study on designing stable microgrids to facilitate higher penetration of solar power generation into a distribution network, considering the small signal stability. The considered microgrid corresponds to an urban community in Colombo City, Sri Lanka. A generalized small signal model was introduced to analyze the stability of an islanded microgrid with dynamic loads, static loads, energy storage, solar photovoltaic (PV) systems, and diesel generator.

The following are the specific conclusions and recommendations:

– Inverter-based microgrids can reduce the system's damping during contingencies and lead to longer oscillations, although most of the reported studies on designing microgrids have considered only the economic factors into the consideration.

– The concept of the stability of dynamic systems can be used to derive a state space model to find the small signal stability of microgrids. A generalized state space model was proposed for a microgrid representing all the important dynamics associated with the distributed energy resources (DERs) compared to the existing stability analysis on microgrids with simplified dynamic models. However, the size of the state matrix and the number of eigenvalues increase with the size of the microgrids. Therefore, stability analysis

of microgrids with high penetration of distributed energy resources is a topic that requires further investigation.
– Participation factor analysis allows the identification of appropriate features of DERs that influence oscillatory and less stable modes of a system. Eigenvalues associated with the inverter-based DERs travel toward the zero-axis with the variation of the load profile. These modes can lead the system into instability. However, the effect of the synchronous machines based DGs on the travel of the eigenvalues is negligible.
– Results of this research revealed that the stability analysis during the design stage of the microgrids for existing distribution networks should not be limited to a single operating point as done by all most all existing studies reported in the literature.
– Rooftop solar-based grid-following inverters can lead to the instability of the system in case of a slight change of voltage at the point of interconnection.
– The penetration level of solar PV has no significant impact on the small signal stability of the microgrids when they operate in grid feeding mode compared to previous studies on droop control-based power sharing with solar PV. However, more research is needed to determine the impact of integrating centralized controls on transient stability and voltage stability.

Acknowledgements

The authors gratefully acknowledge the support provided by the Senate Research Committee University of Moratuwa; Grant number SRC/LT/2020/33 and Manitoba Hydro International by giving the PSCAD professional license.

References

[1] Tran T.Q., *Current limiting algorithm for three-phase grid-connected inverters*, Archives of Electrical Engineering, vol. 71, no. 3, pp. 559–579 (2022), DOI: 10.24425/aee.2022.141671.

[2] Mishra S., Ramasubramanian D., *Improving the small signal stability of a PV-DE-dynamic load-based microgrid using an auxiliary signal in the PV control loop*, IEEE Transactions on Power Systems, vol. 30, no. 1, pp. 166–176 (2015), DOI: 10.1109/TPWRS.2014.2322100.

[3] Rasheduzzaman M., Mueller J.A., Kimball J.W., *Reduced order small-signal model of microgrid systems*, IEEE Transactions on Sustainable Energy, vol. 6, no. 4, pp. 1292–1305 (2015), DOI: 10.1109/TSTE.2015.2433177.

[4] Shuai Z., Peng Y., Liu X., Li Z., Guerrero J.M., Shen Z.J., *Parameter stability region analysis of islanded microgrid based on bifurcation theory*, IEEE Transactions on Smart Grid, vol. 10, no. 6, pp. 6580–6591 (2019), DOI: 10.1109/TSG.2019.2907600.

[5] Mohamad A.M.E.I., Mohamed Y.A.R.I., *Investigation and assessment of stabilization solutions for dc microgrid with dynamic loads*, IEEE Transactions on Smart Grid, vol. 10, no. 5, pp. 5735–5747 (2019), DOI: 10.1109/TSG.2019.2890817.

[6] Majumder R., *Some aspects of stability in microgrids*, IEEE Transactions on Power Systems, vol. 28, no. 3, pp. 3243–3252 (2013), DOI: 10.1109/TPWRS.2012.2234146.

[7] Tang X., Deng W., Qi Z., *Investigation of the dynamic stability of microgrid*, IEEE Transactions on Power Systems, vol. 29, no. 2, pp. 698–706 (2014), DOI: 10.1109/TPWRS.2013.2285585.

[8] Mahdavian A., Ghadimi A.A., Bayat M., *Microgrid small-signal stability analysis considering dynamic load model*, IET Renewable Power Generation, vol. 15, no. 13, pp. 2799–2813 (2021), DOI: 10.1049/rpg2.12203.

[9] Agrawal R., Changan D., Bodhe A., *Small signal stability analysis of standalone microgrid with composite load*, Journal of Electrical Systems and Information Technology, vol. 7, no. 1, pp. 1–20 (2020), DOI: 10.1186/s43067-020-00020-9.

[10] Kahrobaeian A., Mohamed Y.A.R.I., *Analysis and mitigation of low-frequency instabilities in autonomous medium-voltage converter based microgrids with dynamic loads*, IEEE Transactions on Industrial Electronics, vol. 61, no. 4, pp. 1643–1658 (2014), DOI: 10.1109/TIE.2013.2264790.

[11] Amelian S.M., Hooshmand R., *Small signal stability analysis of microgrids considering comprehensive load models - a sensitivity based approach*, in 2013 Smart Grid Conference (SGC), pp. 143–149 (2013), DOI: 10.1109/SGC.2013.6733828.

[12] Han Y. *et al.*, *Small signal stability analysis of microgrid with multiple parallel inverters*, IOP Conference Series: Earth and Environmental Science, vol. 687, no. 1, 012112 (2021), DOI: 10.1088/1755-1315/687/1/012112.

[13] Krismanto A.U., Mithulananthan N., Krause O., *Stability of renewable energy based microgrid in autonomous operation*, Sustainable Energy, Grids and Networks, vol. 13, pp. 134–147 (2018), DOI: 10.1016/j.segan.2017.12.009.

[14] Pulcherio M., Illindala M.S., Choi J., Yedavalli R.K., *Robust microgrid clustering in a distribution system with inverter-based DERs*, IEEE Transactions on Industry Applications, vol. 54, no. 5, pp. 5152–5162 (2018), DOI: 10.1109/TIA.2018.2853039.

[15] Yang C., Huang L., Xin H., Ju P., *Placing grid-forming converters to enhance small signal stability of PLL-integrated power systems*, IEEE Transactions on Power Systems, vol. 36, no. 4, pp. 3563–3573 (2021), DOI: 10.1109/TPWRS.2020.3042741.

[16] Pogaku N., Prodanovic M., Green T.C., *Modeling, analysis and testing of autonomous operation of an inverter-based microgrid*, IEEE Transactions on Power Electronics, vol. 22, no. 2, pp. 613–625 (2007), DOI: 10.1109/TPEL.2006.890003.

[17] Begum M., Li L., Zhu J., Li Z., *State-space modelling and stability analysis for microgrids with distributed secondary control*, IEEE 27th International Symposium on Industrial Electronics (ISIE), pp. 1201–1206 (2018), DOI: 10.1109/ISIE.2018.8433649.

[18] Hamzeh M., Ghafouri M., Karimi H., Sheshyekani K., Guerrero J.M., *Power oscillations damping in dc microgrids*, IEEE Transactions on Energy Conversion, vol. 31, no. 3, pp. 970–980 (2016), DOI: 10.1109/TEC.2016.2542266.

[19] Krismanto A.U., Mithulananthan N., Krause O., *Stability of renewable energy based microgrid in autonomous operation*, Sustainable Energy, Grids and Networks, vol. 13, pp. 134–147 (2018), DOI: 10.1016/j.segan.2017.12.009.

[20] He T., Li S., Wu S., Li K., *Small-signal stability analysis for power system frequency regulation with renewable energy participation*, Mathematical Problems in Engineering, vol. 2021, pp. 1–13 (2021), DOI: 10.1155/2021/5556062.

[21] Ediriweera W.E.P.S., Lidula N.W.A., *Design and protection of microgrid clusters: A comprehensive review*, AIMS Energy, vol. 10, no. 3, pp. 375–411 (2022), DOI: 10.3934/energy.2022020.

[22] Solano J., Rey J.M., Bastidas-Rodríguez J.D.A.I., Hernández A.I., *Stability Issues in Microgrids*, Cham: Springer International Publishing, pp. 287–310 (2019), DOI: 10.1007/978-3-319-98687-6_11.

[23] Majumder R. *et al.*, *Improvement of stability and load sharing in an autonomous microgrid using supplementary droop control loop*, IEEE Transactions on Power Systems, vol. 25, no. 2, pp. 796–808 (2010), DOI: 10.1109/TPWRS.2009.2032049.

[24] Wang S. *et al.*, *A review on the small signal stability of microgrid*, PIEEE 8th International Power Electronics and Motion Control Conference (IPEMC-ECCE Asia), pp. 1793–1798 (2016), DOI: 10.1109/IPEMC.2016.7512566.

[25] Diaz G., Gonzalez-Moran C., Gomez-Aleixandre J., Diez A., *Scheduling of droop coefficients for frequency and voltage regulation in isolated microgrids*, IEEE Transactions on Power Systems, vol. 25, no. 1, pp. 489–496 (2010), DOI: 10.1109/TPWRS.2009.2030425.

[26] Vittal V., Mccalley J.D., Anderson P.M., Fouad A.A., *Power system control and stability*, John Wiley & Sons (2019).

[27] Mon T.W., Aung M.M., *Simulation of synchronous machine in stability study for power system*, International Journal of Electrical and Electronics Engineering, vol. 1, no. 1, pp. 49–54 (2008), online available at: https://www.ematlab.com/paper/dynamic/D24/D24.pdf.

[28] hydro I.M., *Phase Locked Loop (PLL) Component*, Manitoba Hydro International, Technical Report (2020), online available at: https://www.pscad.com/knowledge-base/article/612.

[29] Filipović F., Petronijević M., Mitrović N., Banković B., Kostić V., *A novel repetitive control enhanced phase-locked loop for synchronization of three-phase grid-connected converters*, Energies, vol. 13, no. 1 (2020), DOI: 10.3390/en13010135.

[30] Hu C., Wang Y., Luo S., Zhang F., *State-space model of an inverter-based microgrid*, 3rd International Conference on Intelligent Green Building and Smart Grid (IGBSG), pp. 1–7 (2018), DOI: 10.1109/IGBSG.2018.8393525.

[31] Gong Q., Lei J., *Design of a bidirectional energy storage system for a vanadium redox flow battery in a microgrid with soc estimation*, Sustainability, vol. 9, pp. 441 (2017), DOI: 10.3390/su9030441.

[32] Adelpour M., Hamzeh M., Sheshyekani K., *Comprehensive small-signal stability analysis of islanded synchronous generator-based microgrids*, Sustainable Energy, Grids and Networks (SEGAN), vol. 26, pp. 100444 (2021), DOI: 10.1016/j.segan.2021.100444.

[33] Kundur P., Malik P., *Power System Stability and Control*, McGraw Hill (2022).

[34] Kron G., *Tensor Analysis of Networks*, John Wiley & Sons (1939).